Journal of Materials Science and Chemical Engineering, 2017, 5, 121-128
http://www.scirp.org/journal/msce
ISSN Online: 2327-6053
ISSN Print: 2327-6045

Thermoelectric Properties of Silver Antimonate with Mixed Valency of Antimony

Kensuke Ozawa[1], Hirofumi Kakemoto[2], Hiroshi Irie[1,2*]

[1]Interdisciplinary Graduate School of Medicine and Engineering, University of Yamanashi, Yamanashi, Japan
[2]Clean Energy Research Center, University of Yamanashi, Yamanashi, Japan
Email: *hirie@yamanashi.ac.jp

How to cite this paper: Ozawa, K., Kakemoto, H. and Irie, H. (2017) Thermoelectric Properties of Silver Antimonate with Mixed Valency of Antimony. *Journal of Materials Science and Chemical Engineering*, **5**, 121-128.
http://dx.doi.org/10.4236/msce.2017.51016

Received: December 14, 2016
Accepted: January 13, 2017
Published: January 16, 2017

Abstract

Silver (Ag) and silver antimonate ($AgSbO_3$) composites with different amounts of Sb^{3+} were synthesized by normal sintering with the aim of realizing a thermoelectric material. The electrical conductivity (σ) increased in the sample containing larger amount of Sb^{3+}, whereas Seebeck coefficient (S) decreased. Producing Sb^{3+} caused the generation of oxygen vacancies in the material, and thus the corresponding donor levels are created in the bandgap, providing more conduction electrons. The conductive Ag particles would contribute to the conduction path as bypasses for carrier transport. The thermal conductivity (κ) was slightly lower in the presence of Ag defects in $AgSbO_3$.

Keywords

Thermoelectric Material, Silver Antimonate, Seebeck Coefficient, Electrical Conductivity, Thermal Conductivity

1. Introduction

Thermoelectric (TE) materials have been attracting attention due to their potential for recycling energy using exhausted heat through the thermal-electric conversion effect, generating clean energy without polluting the environment. Recently, several oxides have been recognized as potential thermoelectric materials [1] [2] [3] [4]. TE conversion efficiency is represented by a dimensionless figure of merit, $ZT = S^2\sigma T/\kappa$, where S, σ, κ, and T are the Seebeck coefficient, electrical conductivity, thermal conductivity, and absolute temperature, respectively. From these equations, large S and σ values and a low κ are necessary for high TE performance.

It is known that typical oxides have a low mobility (μ) and high κ (particularly, κ_{ph}, which is the thermal conductivity mediated by phonons), originating from

their ionic bonding between light atoms and high electronegativity of oxygen. Different from these oxides, silver antimonite ($AgSbO_3$), which has a defect pyrochlore structure composed of linear chains of AgO_6 and SbO_6, possesses rather high μ originating from its highly-dispersed valence band and conduction band composed of Ag 5s and Sb 5s orbitals, respectively [5] [6]. In addition, $AgSbO_3$ has low stacking density and thus its κ_{ph} is significantly lower than those of other oxides [7] [8]. So, $AgSbO_3$ has been investigated as a candidate n-type TE material, e.g., by addition of CuO [5] and by using a spark plasma sintering (SPS) method to prepare dense $AgSbO_3$ [7]. According to Wiggers *et al*., aggregated Ag islands are formed in the thermally treated $AgSbO_3$, causing the increase in σ by the electron hopping between such metallic islands [9]. However, the previous studies, regarding TE properties of $AgSbO_3$, did not mention the existence of metallic Ag. Moreover, the valency of Sb (Sb^{3+} ($4d^{10}$), Sb^{5+} ($4d^{10}5s^2$)) should affect σ due to generation of oxygen vacancy in the presence of Sb^{3+}; however such discussion has not been performed. Thus, in the present paper, we characterize the $AgSbO_3$ in details, prepared by the combination of a solid state reaction (SSR) method and a nitric acid (HNO_3) treatment [10]. In addition, the existence of metallic silver and the ratio of Sb^{3+}/Sb^{5+} in $AgSbO_3$ are discussed in connection with σ, S, and κ.

2. Experimental

$AgSbO_3$ was synthesized by SSR using Ag_2O (>99.0%, Kanto Kagaku) and Sb_2O_3 (>98.0%, Kanto Kagaku) as raw materials. The raw materials were weighed to the stoichiometric molar ratio, and were mixed by ball milling (200 rpm, milling rate) for 20 h, and then the mixed powder was calcined at 900˚C for 2 h. The partial calcined powder was uniaxially pressed into a rectangular pellet with the dimensions ~ 4 × 5 × 20 mm, followed by calcination in an electric furnace (HPM-1N, AS-ONE) in air at 900˚C for 2 h (denoted by NS). The remaining calcined powder was washed by HNO_3 (5.0 mol/L, Kanto Kagaku), then dried at 90˚C for 20 h. The obtained powder was pressed into a pellet followed by calcination in the electric furnace under the same conditions, and obtained sample was denoted by NAT-NS.

The obtained calcined powders and sintered bodies, after grounding powders and pulverizing bodies, respectively, into fine powders were characterized by conventional X-ray diffraction analysis (XRD) with CuK_α radiation (PANalytical, PW-1700). Synchrotron radiation powder diffraction patterns were obtained at BL02B2 in SPring-8 after pulverizing bodies into fine powders. The patterns were collected in the 2θ range of 3˚ - 73˚ in a step scanning mode, with a step length of 0.01˚. The Rietveld analyses using a RIETAN-FP software (a multi-purpose pattern-fitting system) were performed on the synchrotron radiation diffraction patterns. For the analysis, the space groups Fd3m (cubic, No. A-227) and Fm-3m (cubic, No. A-225) were used as the starting structural model of $AgSbO_3$ (a = 10.23 nm) and Ag (a = 4.0857 nm). A scanning electron microscope (SEM; JSM-6500F, JEOL) was used to observe the morphology of cross-sectional

surfaces of the samples. The valency of Ag and Sb ions was evaluated by X-ray photoelectron spectroscopy (XPS; Axis-Ultra, Shimadzu).

To measure σ and S, either two or four Pt wires, respectively, were attached by an Ag-conductive region to the prepared rectangular pellet samples. The temperature dependence of S (Yokogawa, Model 7563) with a temperature gradient of 5 - 20 K and that of σ (Agilent Technologies, E5273A) were measured from 473 K to 873 K by conventional two-probe steady-state and four-probe methods, respectively. We then calculated the power factor (PF), as expressed by $S^2\sigma$, for each sample. A modified Harman method was used to measure ZT at 600˚C [11] and then we calculated κ by using the equation, $ZT = S^2\sigma T/\kappa$.

3. Results and Discussion

3.1. Characterizations

The observed diffraction patternsfor NS and NAT-NS by synchrotron radiation are shown in **Figure 1(a)** and **Figure 1(b)**, respectively, and indicated it adopted double phases of cubic $AgSbO_3$ and Ag. Not shown here, but calcined $AgSbO_3$ indicated the homogeneous defect pyrochlore structure by the conventional XRD. The detection of Ag was reasonably expected as Ag_2O is thermally decom-

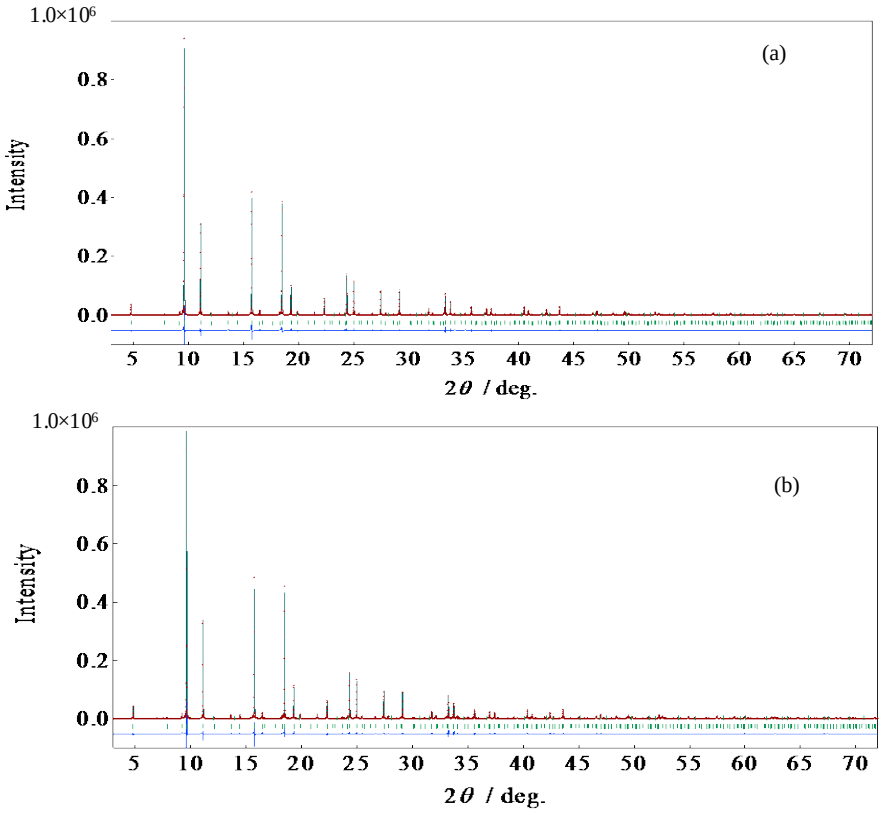

Figure 1. Measured synchrotron radiation diffraction patterns and patterns calculated by Rietveld analysis for the prepared samples, (a) NS and (b) NAT-NS. The dotted red plots, black lines, and blue lines represent measured patterns, calculated patterns, and the differences between the measured and calculated patterns, respectively. Crystallographic data determined by the Rietveld analysis are shown in **Table 1**.

posed to Ag at ~280˚C. Figure 1 also includes the calculatedpattern involving $AgSbO_3$ and Ag, and the difference between the observed and calculated values. The molar percentages of $AgSbO_3$ and Ag in both samples, their lattice parameters, and their compositions were determined by Rietveld refinement and are summarized in Table 1. In the NS sample, the Ag/Sb ratio is unity, in good agreement with the stoichiometric ratio ($Ag_{1.00}Sb_{1.00}O_3$), although Ag exists separately in spite of the stoichiometric ratio of starting materials, Ag_2O and Sb_2O_3. This is reasonable because Sb element volatilized during sintering [5] [8]. In contrast, in the NAT-NS sample, the Ag/Sb ratio is less than unity ($Ag_{0.98}Sb_{1.00}O_3$), reflecting the HNO_3 treatment which extracted Ag from the $AgSbO_3$lattice, causing the Ag defect in $AgSbO_3$. The amounts of the separated Ag in both samples were observed to be similar. The relative densities of NS and NAT-NS pellets were also quite similar, 58.9 and 56.6%, respectively (Table 2). Those values were small, ~60% of the theoretical ones, which is considered to be attributable to the evaporation of Sb [5].

SEM images of the fracture surfaces of NS and NAT-NS are shown in Figure 2(a) and Figure 2(b), respectively. The NS and NAT-NS powders, with particle sizes of ~100 - 200 nm in diameter, appeared to be aggregated, indicating that both of them were porous. The binding energies corresponding to Ag $3d_{5/2}$ of Ag^0 (Ag), Ag^+ (Ag_2O), and Ag^{2+} (AgO) are quite similar, and are 368.0 - 368.3, 367.6 - 367.8, and 367.3 - 367.4 eV, respectively [12]. Since all the energies are in such a narrow range, it is quite difficult to perform a quantitative analysis of the Ag oxidation states from a deconvolution analysis of XPS spectra with high certainty. However, qualitatively, as shown in Figure 3(a), the spectrum peak of HNO_3-treated sample (NAT-NS) shifted to the higher binding energy side (inset in Figure 3(a)), and also the spectrum had tailing in the lower binding energy region. These observations indicate that the HNO_3-treated sample has more Ag

Table 1. Crystallographic data determined by the Rietveld analysis.

Sample	NS	NAT-NS
R_{wp}	8.90	10.1
S	6.19	6.86
Ag content/mol%	0.79	0.83
Lattice parametrt of Ag, *a*/nm	4.078	4.081
Lattice parametrt of $AgSbO_3$, *a*/nm	10.22	10.25
Composition of $AgSbO_3$[a]	$Ag_{1.00}Sb_{1.00}O_3$	$Ag_{0.98}Sb_{1.00}O_3$

a. Estimated from the occupancies of Ag and Sb in $AgSbO_3$.

Table 2. Characterization data of NS and NAT-NS, SPS samples.

Sample	NS	NAT-NS
Relative density/%	58.9	56.6
Sb^{3+}/Sb^{5+} ratio	1.5	0.23

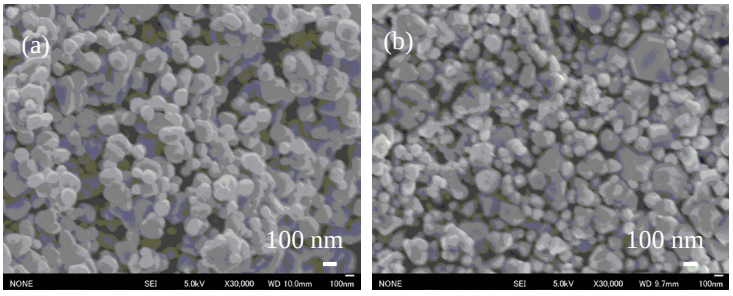

Figure 2. Cross-sectional SEM images of (a) NS and (b) NAT-NS.

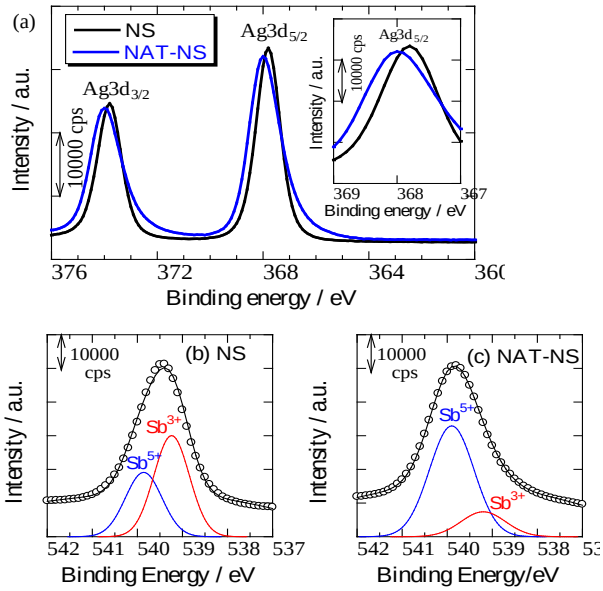

Figure 3. XPS spectra for (a) Ag 3d (Ag $3d_{3/2}$, Ag $3d_{5/2}$), Sb $3d_{3/2}$ of (b) NS and (c) NAT-NS. The plotted experimental data and the fitted curves (black lines) closely coincided. The deconvolution curves of Sb^{3+} (red lines) and Sb^{5+} (blue lines) are included. The Sb 3d peaks were calibrated using the C 1s peak derived from the hydrocarbon surface contaminant with a binding energy of 284.6 eV. The Sb^{3+}/Sb^{5+} ratios obtained from the peak deconvolution are described in **Table 2**.

in $AgSbO_3$ including Ag^0 and Ag^{2+} oxidation states. The Sb $3d_{3/2}$ XPS spectra of NS and NAT-NS are shown in **Figure 3(b)** and **Figure 3(c)**, respectively. As for the oxidation states of Sb, the peaks at 540.7 and 539.7 eV are assigned to the $3d_{3/2}$ orbital of Sb^{5+} and Sb^{3+}, respectively [13]. To quantitatively evaluate the Sb^{3+}/Sb^{5+} atomic ratios, peak deconvolution was performed using a Gaussian lineshape. The component Sb^{3+} and Sb^{5+} spectra determined by deconvolution and fitted peaks are also shown in **Figure 3(b)** and **Figure 3(c)**. The atomic ratios of Sb^{3+}/Sb^{5+}, which were determined by the area of Sb $3d_{3/2}$ for Sb^{3+} divided by thatfor Sb^{5+}, are also shown in **Table 2**. When we compare the Sb^{3+}/Sb^{5+} ratio between NS and NAT-NS, the amount of Sb^{5+} increased after HNO_3 treatment. This is also reasonable because HNO_3 acts as an oxidant. So, it could be considered that Ag^{2+} also increased, and then Ag^0 in $AgSbO_3$ might increase to maintain charge neutrality (**Figure 2** & **Figure 3**).

3.2. Thermoelectric Properties

Figure 4(a) shows the temperature dependence of σ for NS and NAT-NS. The σ values of both samples increased with increasing temperature, which is typical semiconductor behavior. In Figure 4(a), NS containing larger amount of Sb^{3+} with the similar amount of the separated Ag, compared to NAT-NS, indicated the higher σ. So, producing Sb^{3+} is the key to increase σ. This could be plausible because generating Sb^{3+} caused the generation of more oxygen vacancies in the material, and thus the corresponding donor levels are created in the band gap. This can provide more conduction electrons than in the case of no donor levels in the gaps. It should be noted that the Sb^{3+}/Sb^{5+} ratio did affect σ more greatly than the Ag/Sb ratio. As mentioned above, NAT-NS containing Ag-defect ($Ag_{0.98}Sb_{1.00}O_y$) has more amounts Ag^0 ($4d^{10}5s^1$) and Ag^{2+} ($4d^9$), meaning the increase in σ due to their open electronic-shell configurations than NS ($Ag_{0.98}Sb_{1.00}O_y$, Ag^+ ($4d^{10}$), closed electronic-shell configuration). However, the opposite experimental results were observed.

Temperature dependence of S for NS and NAT-NS is shown in Figure 4(b). S values of both samples were negative, indicating the occurrence of n-type conduction. The trend of the absolute values of S almost covers the Ioffe's theory, that is, the absolute value of S decreases when σ increases. So, NAT-NS had the higher absolute values of S. Figure 4(c) shows the temperature dependence of power factor (PF), which was calculated from the formula $\sigma \times S^2$. The PF observed in this study ($\sim 1 \times 10^{-5}$ $W \cdot m^{-1} \cdot K^{-2}$) was obtained for NS at 600˚C.

Finally, we examined the value of ZT for the NS and NAT-NS samples at 600˚C using the modified Harman method and then κ was calculated. The ZT values for NS and NAT-NS were 0.009 and 0.007, respectively. The κ value for NS was calculated to be 0.42 $W \cdot m^{-1} \cdot K^{-1}$, which is reasonably consistent with the previously reported values of 1.1 and 0.8 $W \cdot m^{-1} \cdot K^{-1}$ at room temperature and

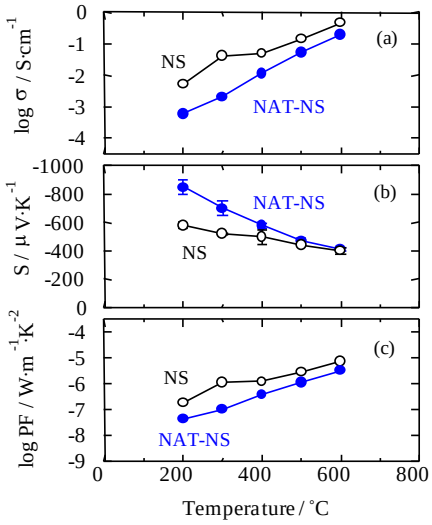

Figure 4. Temperature dependence of (a) electrical conductivity, σ and (b) Seebeck coefficient, S, and (c) power factor (PF) for NS and NAT-NS samples.

400˚C, respectively [8]. The κ value for NAT-NS was 0.38 $W \cdot m^{-1} \cdot K^{-1}$, which is slightly smaller than that for NS. This might be attributable to the presence of Ag defects, causing the phonon scattering by the defect site. Although these *ZT* values need to be increased by around two orders of magnitude to be suitable for practical use, this study provides that the introduction of Sb^{3+} in $AgSbO_3$ enhanced the thermoelectric property.

4. Conclusion

We prepared $AgSbO_3$-based thermoelectric materials with and without the HNO_3 treatment. Then the sample that had higher σ indicated the higher *Z*, attributable to the generation of Sb^{3+}, in spite of smaller *S* and larger κ. The *ZT* value for NS was observed to be ~0.009 at 600˚C, which is two orders of magnitude smaller than the minimum value considered being required for practical use, which is greater than 1. To achieve a higher *ZT* value, we are now trying to prepare dense $AgSbO_3$ with and without HNO_3 treatment using the SPS method because it is well-known that the SPS method allows the production of dense samples, resulting in the enhanced TE properties.

Acknowledgements

The experiments at SPring-8 were performed with the approval of the Japan Synchrotron Radiation Research Institute (JASRI) (Proposal No. 2014A1008).

References

[1] Terasaki, I., Sasago, Y. and Uchinokura, K. (1997) Large Thermoelectric Power in $NaCo_2O_4$ Single Crystals. *Physical Review B*, **56**, R12685-R12687. https://doi.org/10.1103/PhysRevB.56.R12685

[2] Ohtaki, M., Tsubota, T., Eguchi, K. and Arai, H. (1996) High-Temperature Thermoelectric Properties of $(Zn_{1-x}Al_x)O$. *Journal of Applied Physics*, **79**, 1816.

[3] Li, S., Funahashi, R., Matsubara, I., Ueno, K., Sodeoka, S. and Yamada, H. (2000) Synthesis and Thermoelectric Properties of the New Oxide Materials $Ca_{3-x}Bi_xCo_4O_{9+\delta}$ $(0.0 < x < 0.75)$. *Chemistry of Materials*, **12**, 2424-2427. https://doi.org/10.1021/cm000132r

[4] Ohta, H., Kim, S., Mune, Y., Mizoguchi, T., Nomura, K., Ohta, S., Nomura, T., Nakanishi, Y., Ikuhara, Y., Hirano, M., Hosono, H. and Koumoto, K. (2007) Giant Thermoelectric Seebeck Coefficient of a Two-Dimensional Electron Gas in $SrTiO_3$. *Nature Materials*, **6**, 129-134. https://doi.org/10.1038/nmat1821

[5] Nishiyama, S., Ichikawa, A. and Hattori, T. (2004) Theromoelectric Properties of CuO-Added $AgSbO_3$ Ceramics. *Journal of the Ceramic Society of Japan*, **112**, 298-300. https://doi.org/10.2109/jcersj.112.298

[6] Allen, J.P., Nilsson, M.K., Scanlon, D.O. and Watson, G.W. (2011) Comparison of the Defective Pyrochlore and Ilmenite Polymorphs of $AgSbO_3$ Using GGA and Hybrid DFT. *Physical Review B*, **83**, Article ID: 035207. https://doi.org/10.1103/PhysRevB.83.035207

[7] Sang, H.-Y. and Li, J.-F. (2010) Thermoelectric Properties of $AgSbO_3$ with Defect Pyrochlore Structure. *Journal of Alloys and Compounds*, **493**, 678-682. https://doi.org/10.1016/j.jallcom.2009.12.190

[8] Li, F. and Li, J.-F. (2011) Microstructure and Thermoelectric Properties of $AgSbO_3$ Ceramics Prepared by Ion-Exchange Powder Synthesis and Normal Sintering. *Journal of Electronic Materials*, **40**, 1035-1041. https://doi.org/10.1007/s11664-011-1525-0

[9] Wiggers, H., Simon, U. and Schon, G. (1998) Conductivity Studies on $AgSbO_3$ Channel Structure by Impedance Spectroscopy. *Solid State Ionics*, **107**, 111-116. https://doi.org/10.1016/S0167-2738(97)00518-3

[10] Kobayashi, R., Tanigawa, S., Takashima, T., Ohtani, B. and Irie, H. (2014) Silver-Inserted Heterojunction Photocatalysts for Z-Scheme Overall Pure-Water Splitting under Visible-Light Irradiation. *The Journal of Physical Chemistry C*, **118**, 22450-22456. https://doi.org/10.1021/jp5069973

[11] Kawano, T., Kakemoto, H. and Irie, H. (2015) Niobium(V) Oxide with Added Silver as a Thermoelectric Material Prepared by Spark Plasma Sintering. *Materials Letters*, **156**, 94-97. https://doi.org/10.1016/j.matlet.2015.04.148

[12] Melin, E.P., Diaz, O.G., Rodrigues, J.M.D., Colon, G. and Navio, G.C. (2012) Effect of Deposition of Silver on Structural Characteristics and Photoactivity of TiO_2-Based Photocatalysts. *Applied Catalysis B*: *Environmental*,**127**, 112-120. https://doi.org/10.1016/j.apcatb.2012.08.007

[13] Zhang, H., Sun, K., Feng, Z., Ying, P. and Li, C. (2006) Studies on the SbO_x Species of SbO_x/SiO_2 Catalysts for Methane-Selective Oxidation to Formaldehyde. *Applied Catalysis A*: *General*, **305**, 110-119. https://doi.org/10.1016/j.apcata.2006.02.038